ROYAL SOCIETY
OF CHEMISTRY

PAPER

Check for updates

Surface and bulk properties of black, blue and transparent TiO$_x$ thin-film photoanodes for green hydrogen generation by water splitting

Katarzyna Płacheta, [ID] [a] Matthijs A. van Spronsen, [ID] [b] Pilar Ferrer, [ID] [b] Marta Radecka [ID] [a] and Katarzyna Zakrzewska [ID] *[c]

This study focusses on the surface and bulk properties of Ti−O thin film photoanodes for water splitting to generate green hydrogen. Here, TiO$_x$ thin films were deposited by reactive RF magnetron sputtering of Ti in an Ar + O$_2$ atmosphere. The oxygen flow rate η_{O_2}, was varied to grow a sequence of TiO, Ti$_2$O$_3$ and TiO$_2$ layers, as determined by X-ray diffraction. The spectral dependence of the optical absorption coefficient reveals a significant colour evolution, which is due to the interference of light, as well as black appearance, resulting from strong absorption within the visible range. Electrical resistivity from impedance spectroscopy increased from 5.2×10^{-2} for black TiO ($\eta_{O_2} = 5\%$) to 9×10^4 ohm cm for transparent anatase TiO$_2$ ($\eta_{O_2} = 30\%$). X-ray photoelectron spectra were collected at different photon energies, 200 and 1200 eV above the O 1s and Ti 2p core levels, probing the surface and subsurface states, respectively. The depth distribution of the OH−Ti^{3+} defects indicated their increased surface/subsurface concentration at higher η_{O_2}. X-ray absorption spectroscopy (XAS) showed that the crystal field splitting increased from 1.7–2.1 eV to 2.2–2.3 eV as the amount of Ti^{3+} states decreased from 20% to 10%. Surface photovoltage (SPV) and the photoelectrochemical performance were correlated. The anatase/rutile mixture or pure anatase TiO$_2$ photoanodes with the highest SPV values of about 270 mV demonstrated the best combination of high negative flat band potential (−650 mV), photocurrent density (350 μA cm^{-2} at 0 V *vs.* Ag/AgCl) and a reasonable shape factor (0.75). These findings highlight the critical role of surface-sensitive characterization in optimizing TiO$_x$ photoanodes for efficient solar-driven hydrogen development.

Introduction

The high surface-to-volume ratio of metal-oxide thin films plays an extremely important role in photocatalytic and photoelectric applications such as water splitting.[1–9] Differentiation between surface and bulk properties and their respective contributions towards the mechanisms of photocatalysis and photoelectrochemical phenomena is a fundamental issue to be resolved. Surface-sensitive methods such as X-ray photoelectron spectroscopy (XPS) and X-ray absorption spectroscopy (XAS) in total electron yield mode (TEY) allow one to study the electronic structure and oxidation/reduction processes even *in situ*. However, the conclusions of these studies are quite frequently extended to describe the properties of a thin film as a whole. Such an approach is unjustified as it leads to misinterpretation of the results. It is therefore crucial to realize that even small differences between the surface and bulk properties of

photoanodes might largely affect their performance. Application of the same method but in a modified configuration such as XAS in total fluorescence yield mode (TFY) in conjunction to TEY is proposed to address this issue.

This work is focussed on TiO$_x$ thin films, which are highly promising photoanodes in photoelectrochemical cells for "green" hydrogen generation, as can be seen in Fig. 1. The number of scientific reports on titanium oxides has been increasing steadily over the last 30 years, of which less than 45% are devoted to thin films and only 1% of them employs synchrotron radiation in the measurements. Titanium dioxide has been chosen due to its exceptional properties such as high photocatalytic activity, good chemical stability and nontoxicity.[10–14] However, stoichiometric, white TiO$_2$ powders and transparent thin films suffer from a profound mismatch between their wide band gap (3.0–3.2 eV) and the solar spectrum, resulting in too low absorption of sunlight in the visible range of wavelengths.[14,15] Diverse schemes such as cation or anion doping, co-doping, and creation of oxygen non-stoichiometry have been proposed to shift the absorption spectrum towards the visible region.[16–20] Numerous attempts to avoid the energetic mismatch inevitably led to deterioration of

[a] Faculty of Materials Science and Ceramics, AGH University of Krakow, Poland
[b] Diamond Light Source Ltd., Didcot OX11 0DE, UK
[c] Faculty of Computer Science, Electronics and Telecommunication, AGH University of Krakow, Poland. E-mail: zak@agh.edu.pl
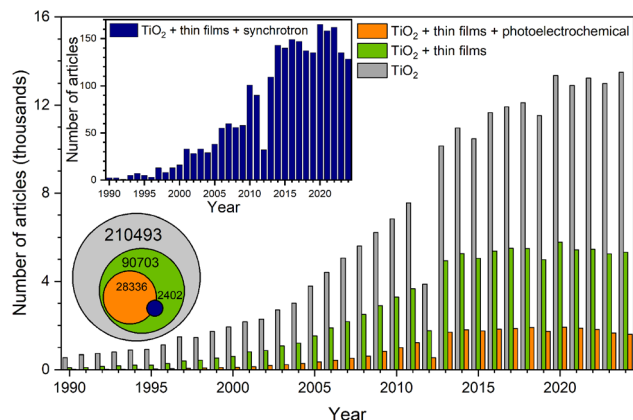
This journal is © The Royal Society of Chemistry 2025

J. Mater. Chem. A, 2025, **13**, 30191–30203 | **30191**

Fig. 1 Number of research articles on "TiO$_2$", "TiO$_2$ + thin films", "TiO$_2$ + thin films + photoelectrochemical" and "TiO$_2$ + thin films + synchrotron" (inset) between 1990 and 2024 (Scopus, 28.04.2025; search in: title, keywords, abstract).

the photocarrier dynamics. This dynamic mismatch is due to the substantial difference between the lifetime of photogenerated charge carriers and time necessary to run the redox reactions at the photoanode–electrolyte interface.[21]

Actually, there is no clear prescription for how to reach a sufficient level of conversion efficiency for hydrogen evolution in the case of TiO$_2$. This problem is far from being solved successfully; hence, it requires a much closer look at the defect and electronic structure.

The photoelectrochemical performance of photoanodes based on TiO$_2$ thin films critically depends on their morphology and thickness as well as the crystallographic and electronic structures.[22] Moreover, much work is still needed to understand the role of surface and bulk properties of this model semiconductor, especially in photocatalysis and photoelectrochemistry.

The idea to apply disordered black or blue titania in photocatalysis or photoelectrochemistry is not a new one, as demonstrated in recently published excellent reviews.[23,24] However, it is debatable whether the positive effect on their performance is due to the introduction of defect states within the fundamental band gap, which are then responsible for light absorption over the visible range.

The term "black TiO$_2$" was proposed for the first time by Chen et al.[25] in 2011. The black appearance of TiO$_2$ that contrasted with its usual white colour, was achieved by hydrogenating titanium dioxide nanocrystals. In their work,[25] an approach to enhance absorption of visible light was proposed by introducing disorder in the TiO$_2$ surface layers. In 2016, Zhang et al.[26] demonstrated a phase selective conversion of mixed anatase/rutile P-25 into ordered anatase (A$_O$) and disordered rutile (R$_D$) blue TiO$_2$ (BTO-I). Three years later, a mixed disordered anatase/ordered rutile (A$_D$/R$_O$) blue TiO$_2$ (BTO-II) was reported.[27] The excellent photocatalytic properties of blue TiO$_2$ BTO-II with a defective anatase phase A$_D$ were explained as follows. The disordered anatase phase absorbs visible light, while the crystalline rutile phase provides fast charge separation. Although the terms black or blue TiO$_2$ are related to the

presence of defects at the surface or in a certain TiO$_2$ phase, disordered titanium dioxide can, in fact, have various colours. For thin films, film thickness has a significant effect on the transmittance and reflectance spectra. Multiple interferences of light reflected from the film–air and the film–substrate interfaces are responsible for the oscillatory character of the transmittance and reflectance spectra. Consequently, the interference results in coloured TiO$_2$, such as blue, violet, green or yellow, while a dark brown or black appearance is the result of strong absorption of electromagnetic radiation within the visible range. The strong light absorption may originate from the formation of mid-gap states, related to defects.[24]

Both bulk and surface properties are important for the photoelectrochemical splitting of water into hydrogen and oxygen. However, one should keep in mind that the first step of the process, i.e., the formation of a semiconductor–electrolyte interface in the dark, leads to band bending, and this effect is sensitive to the electronic structure of the semiconductor surface. Light absorption in deeper layers depends on the penetration depth, which is inversely proportional to the absorption coefficient. Finally, transport of the photogenerated charge carriers, depending on the depth at which they are formed, is mediated by the bulk properties of the semiconducting thin films.

Therefore, we intend to demonstrate that a certain combination of experimental methods that make use of synchrotron radiation such as XPS at different photon energies along with XAS in TEY and TFY modes will allow us to differentiate between the electronic structures of the bulk vs. the surface. Specifically, this work focuses on thin films deposited by reactive magnetron sputtering under intentionally varied oxygen content in the Ar + O$_2$ gas mixture. Our studies cover the full range, starting from TiO, via Ti$_2$O$_3$, fine rutile, a mixture of rutile and anatase, finally reaching pure anatase TiO$_2$. To the best of our knowledge, systematic studies of the role of surface and bulk properties of the Ti–O system in the form of thin films in green hydrogen generation have not been performed so far.

Experimental

Thin film deposition by magnetron sputtering

Thin films were deposited via reactive RF magnetron sputtering in an ultra-high vacuum (UHV) system (PREVAC) from a metallic 2″ Ti target (99.995% purity, Kurt J. Lesker) in a mixed flow-controlled O$_2$ + Ar atmosphere. The base pressure in the processing chamber was typically 10^{-8} mbar. Substrates (amorphous silica Q – Continental Trade, glass coated with conductive indium–tin oxide (ITO) – Sigma-Aldrich, titanium foil, silicon wafers – Si-Mat Silicon Materials) were sonicated for 10 minutes in each of the five following cleaning liquids: water with detergent, water, deionized water, acetone and isopropanol to remove contamination. The cleaned substrates were mounted onto a 2″ sample holder (PTS, PREVAC) and loaded into a vacuum chamber, where they were bombarded with Ar$^+$ ions for 10 minutes at 10 mA/3 kV prior to sputtering. During the entire deposition process the substrates were heated to 350 °C and rotated at 8 rpm to provide uniform film growth.

30192 | J. Mater. Chem. A, 2025, **13**, 30191–30203

This journal is © The Royal Society of Chemistry 2025

The ignition of the glow discharge required operating pressures within the range of $(1.4–1.6) \cdot \times 10^{-2}$ mbar. This was maintained by introducing an Ar + O_2 gas mixture at a constant flow rate of 40 sccm.

To grow thin films with a composition covering the full range from TiO to TiO_2, the O_2 flow rate was varied while keeping the total flow constant. The relative oxygen flow ratio η_{O_2} is defined according to eqn (1) as:

$$\eta_{O_2} = \frac{\text{flow rate}(O_2)}{\text{flow rate}(O_2 + Ar)} \times 100\% \tag{1}$$

This parameter was introduced as a technological variable and was varied from $\eta_{O_2} = 5\%$ for TiO to $\eta_{O_2} = 30\%$ for pure anatase TiO_2. This resulted in O_2 partial pressures, p_{O_2} within the range of $(1.5–9.5) \times 10^{-4}$ mbar.

Film thickness was controlled by deposition time while keeping the target power density at 10 W cm^{-2}. At the highest η_{O_2} of 25–30%, the power density was raised to 12 W cm^{-2} in order to compensate for a substantial decrease in the sputtering rate due to the well-known target poisoning,[28] attributed to the oxidation of the target surface.

Basic characterization methods

The film thickness was measured with a mechanical surface profilometer (Talystep, Rank Taylor Hobson) after the deposition. Surface and cross-sectional images, taken by means of a scanning electron microscope (Xe-PFIB Helios G4 PFIB CXe, Thermo Fisher Scientific), helped to verify the results obtained by mechanical profiling and allowed for studying the microstructure of the films. The film thickness obtained from profilometry was confirmed by the interpretation of the optical transmittance and reflectance spectra within the wavelength range in which the interference was observed. Moreover, the analysis of the optical data recorded over the UV-vis-IR range, *i.e.*, from 200 to 3200 nm, by means of a double beam Lambda 19 spectrophotometer (PerkinElmer) allowed for determination of the absorption coefficient according to the method described in ref. 29 and 30.

The electrical conductivity, σ, of the thin films was estimated from electrochemical impedance spectroscopy (EIS), for which the films were deposited onto ITO substrates. EIS measurements were performed at room temperature in air over the frequency range of $1–10^6$ Hz at 10 mV amplitude with a Solartron 1260 system, including a dielectric interface 1294. The measured spectra were analysed using ZView software. The model used to fit the experimental spectra included an equivalent circuit consisting of a resistor (R) and a constant phase element (CPE) in parallel. The conductivity values were obtained on the basis of the resistance, film thickness and electrode distance.

The crystal structure was characterized by grazing incidence X-ray diffraction (GIXRD) by means of an X'Pert MPD diffractometer (Philips) equipped with a Cu K$_\alpha$ X-ray source (wavelength of 0.154 nm). Data at different incidence angles (0.5–2°) were compared with reference patterns from the International Centre for Diffraction Data to identify phases.

Surface *vs.* bulk characterization with synchrotron radiation

X-ray photoelectron spectroscopy (XPS) and X-ray absorption spectroscopy (XAS) experiments were carried out at the Diamond Light Source Ltd. (United Kingdom).[31] XPS spectra were collected at B07-B (ES-1: High Throughput UHV XPS). The pass energy was set to 20 eV, and the energy step was 0.1 eV. To probe the surface at different depths, O 1s and Ti 2p spectra were collected at photon energies of 200 eV and 1200 eV above the O 1s (530 eV) and Ti 2p (460 eV) core levels. Carbon 1s spectra were recorded for all samples at four photon energies: 730, 1730, 660 and 1660 eV (Fig. S1, in the SI) to calibrate O 1s and Ti 2p spectra, which were charge-referenced to unfunctionalized, saturated carbon 1s peak (C–C) at 285.0 eV and fitted with Gaussian profiles after Shirley background subtraction using OriginLab software.

XAS was performed in two different modes, *i.e.*, surface sensitive, total electron yield (TEY), and total fluorescence yield (TFY) for bulk characterization, at beamline B07-B (ES-2: Ambient Pressure NEXAFS). The energy ranges extended from 450 to 490 eV for the Ti $L_{2,3}$ edge and from 525 to 560 eV for the O K edge. The XAS spectra were measured using a 600 l mm^{-1} grating with the exit slits set to 0.025 and 0.05 mm for O K and Ti $L_{2,3}$, respectively. The energy resolution was 25 meV. The measurements were performed at room temperature under vacuum (at a pressure of 10^{-5} mbar). The fluorescence yield was detected using a photodiode covered with 40 nm-thick Al foil to avoid damage. The X-ray beam was normal to the film surface.

Interaction with light – CPD from Kelvin probe and photocurrent measurements

The contact potential difference (CPD) was recorded as a function of time at room temperature under ambient pressure in a dark environment and upon UV illumination ($\lambda = 370$ nm) to determine the surface photovoltage (SPV). Thin films deposited onto titanium foil were analysed using a Kelvin probe (Kelvin Probe 4.0, Instytut Fotonowy) equipped with a Faraday cage. Each CPD value was calculated from the intersection of the current *vs.* backing potential plot, at 3 different distances (0.4, 0.6 and 0.8 mm) between the oscillating Kelvin probe tip (Au mesh, 2.5 mm diameter) and the sample surface within the backing potential range of -2.0 to $+1.0$ V (Fig. S2 in the SI). The illumination source was a LED revolver (Instytut Fotonowy) with a maximum light power of 76.5 mW at 370 nm, equipped with an optical fibre to illuminate the sample directly.

Photocurrent measurements in the dark and under white light illumination (290 mW) were performed in a self-made photoelectrochemical cell (PEC) comprising three electrodes: a working electrode based on titanium oxide thin films, a counter electrode (black Pt) and a reference silver–silver chloride electrode in saturated KCl (Ag/AgCl). The reference electrode is required in PEC testing in order to measure the potential of the working electrode on a well-defined electrochemical scale. The Ag/AgCl reference electrodes can generally be used over a wide range of pH values. PEC cells use light-transparent electrolytes in which there is no light-induced

This journal is © The Royal Society of Chemistry 2025

J. Mater. Chem. A, 2025, **13**, 30191–30203 | **30193**

excitation of redox-active species. The electrodes were immersed in 0.8 M Na_2SO_4(aq) electrolyte of pH = 6.9.

The selection of the electrolyte is crucial to ensure that the semiconductor working electrode does not undergo corrosion when immersed in solution. Illumination of the working electrode with a xenon lamp enables photocurrent detection. A potential difference was applied, and the photocurrent was measured using a potentiostat (MTM Anko M161E), in combination with the EALab program. The current–voltage characteristics of the system with and without illumination gives information on important parameters, such as the flat-band potential, as well as shape and fill factors that determine the photoanode or photocathode performance in the PEC.

Results and discussion

Results of basic characterization methods

Differences in the optical properties, including the spectral dependence of the transmittance $T(\lambda)$ and reflectance $R(\lambda)$ coefficients, can explain the colour change from black to transparent of the deposited TiO_x thin films (Fig. 2). Tuning of these optical parameters can be achieved by changing the ratio of oxygen to argon during film growth as already observed before.[32–34] At low oxygen-to-argon flow rates (below 10%), TiO and Ti_2O_3 crystallize as indicated by their X-ray diffraction patterns (Fig. S3, in the SI). They both appear black due to their transmittance, $T(\lambda)$, not exceeding 20% within the visible light range. These films are relatively well conducting with electrical conductivity on the order of 10–20 $(\Omega\,cm)^{-1}$ as determined from EIS.

Blue, defective TiO_2 is synthesized at $p_{O_2} = 4.1 \times 10^{-4}$ mbar as shown in Fig. 2 and S4. Its transmittance spectrum indicates a fundamental absorption edge corresponding to rutile. However, according to XRD the rutile crystallites are quite small; that is why this sample is referred to as "fine" rutile. Its electrical resistivity of 18 ohm cm is almost three orders of magnitude lower than that of well-crystallized, anatase TiO_2. This value is typical for defective titania with a near-stoichiometric composition. The transition to well crystallized, transparent rutile occurs at $p_{O_2} = 4.4 \times 10^{-4}$ mbar, while at higher η_{O_2} a mixture of rutile and anatase appears. At the highest $p_{O_2} = 9.5 \times 10^{-4}$ mbar pure anatase is formed.

The regular oscillations observed in transmittance and reflectance coefficients as functions of wavelength, λ, can be explained by light interference as the thickness of the transparent films is comparable to the λ. Considering T and R, as well as the film thickness, d, the absorption coefficient α, was calculated from eqn (2):

$$\alpha = \frac{1}{d}\,\ln\left(\frac{100 - R}{T}\right) \qquad (2)$$

The obtained absorption coefficient α shows a strong dependence on the wavelength (Fig. S4, in the SI). For further analysis, 375 nm light (corresponding to $h\nu = 3.3$ eV, *i.e.*, comparable to the band gap of TiO_2) was chosen (Fig. 3a).

The absorption coefficient systematically decreases with an increase in η_{O_2} while the electrical resistivity demonstrates the opposite behaviour (Fig. 3a). Therefore, in this work we propose a figure of merit ϕ_M as a parameter to characterize titanium oxide thin films, combining the electrical and optical properties (eqn (3)):

$$\phi_M\ [nm] = \frac{\log \rho/\rho_0}{100\alpha\ [nm^{-1}]} \qquad (3)$$

where ρ is the electrical resistivity and $\rho_0 = 10^{-7}$ ohm cm.

This parameter was chosen instead of technological ones such as oxygen partial pressure or flow rate during sputtering because both of them affect the mean free path of particles in the chamber. Despite the same value of η_{O_2}, the properties of thin films are not comparable.

The figure of merit, ϕ_M, for thin films deposited at η_{O_2} values ranging from 5 to 30% is presented in Fig. 3b and further serves as a parameter distinguishing the deposited samples. Fundamental properties of the deposited thin films such as thickness d, phase composition and electrical conductivity σ along with the identification code of the samples ϕ_M (figure of merit defined by eqn (3)) are provided in Table S1.

Fig. 2 Transmittance (blue) and specular reflectance (red) coefficients as a function of photon energy ($h\nu$) for titanium oxide thin films obtained at different oxygen partial pressures p_{O_2}; conductivity at room temperature (σ) calculated from EIS measurements, thickness (d) and photographs of thin films deposited on amorphous silica substrates (dimensions 18 × 25 mm). In the inset: transmittance spectrum for TiO thin films.

Results of surface *vs.* bulk characterization with synchrotron radiation

The comparison between X-ray photoelectron and X-ray absorption spectra, XPS and XAS, can be followed in Fig. 4.
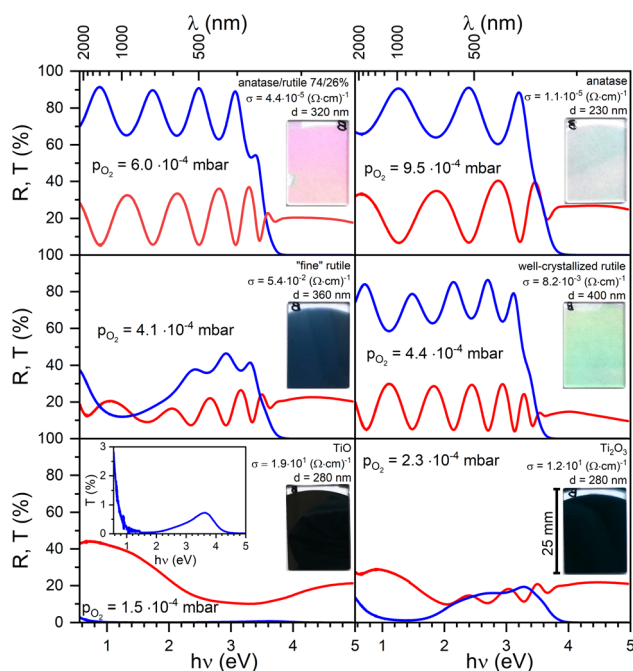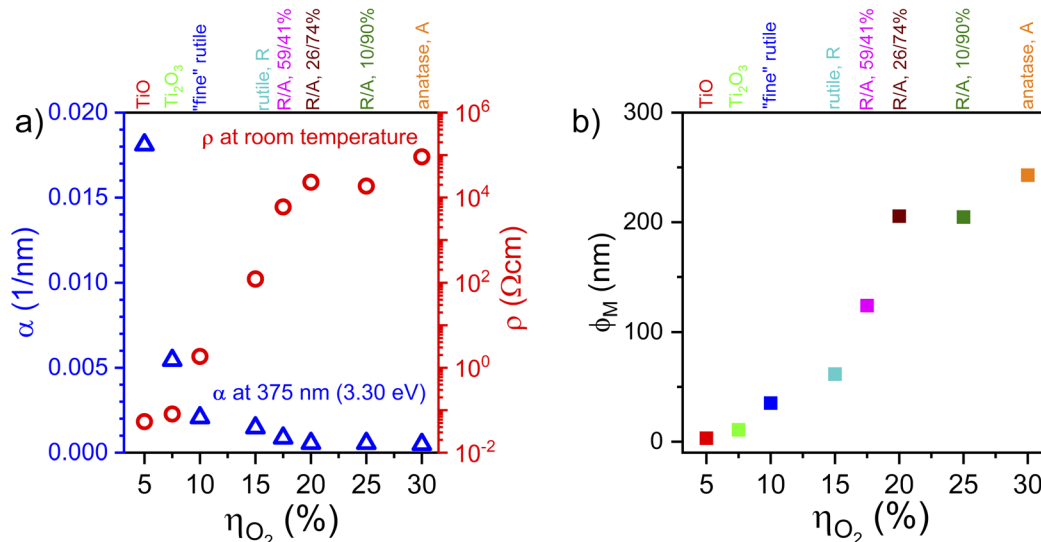
30194 | *J. Mater. Chem. A*, 2025, **13**, 30191–30203

This journal is © The Royal Society of Chemistry 2025

Fig. 3 Absorption coefficient (blue triangles) at $\lambda = 375$ nm ($h\nu = 3.30$ eV), electrical resistivity (red circles) from electrochemical impedance spectra measured at room temperature for titanium oxide thin films sputtered at different oxygen flow ratios η_{O_2} and oxygen partial pressures p_{O_2} (a), and figure of merit (ϕ_M) of thin films with different crystallographic structures calculated from eqn (3) (b).

XPS probes the occupied core levels while XAS involves electron transitions to unoccupied valence states as shown in Fig. 4a (ref. 35 and 36). Both methods are useful for the electronic structure determination in the case of thin films.[37,38] Chemical and electronic states at the surface were evaluated based on X-ray photoelectron spectroscopy (XPS) measurements.

X-ray photoelectron spectroscopy (XPS) as a surface technique is limited to a few uppermost layers. The synchrotron radiation (SR) based sampling depth l_s for XPS within the soft X-rays range was estimated after Flavell[39] according to eqn (4):

$$l_s = 3\Lambda \cos\theta \qquad (4)$$

where θ is the angle between the surface normal and the direction of the emitted photoelectrons leaving the sample (in this work $\theta = 0$) and Λ is the inelastic mean free path (IMFP) of
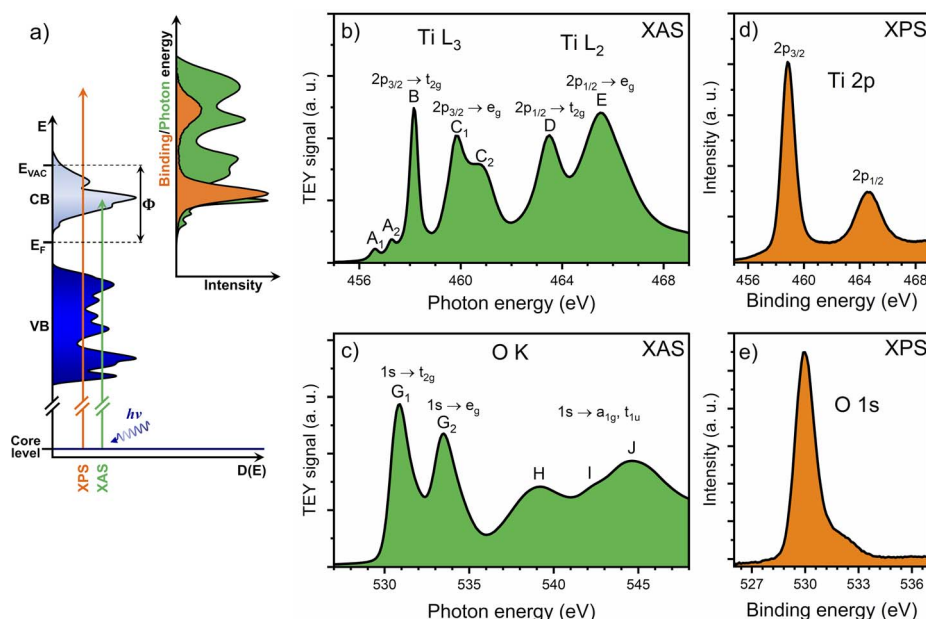

Fig. 4 Schematic diagram (adapted from ref. 35 and 36) of transitions resulting in X-ray photoelectron (orange) and X-ray absorption (green) applied to the spectra of titanium dioxide from our work; VB and CB denote valence and conduction bands, E_F is the Fermi level, Φ – work function, E_{VAC} – vacuum level, and $h\nu$ is the photon energy within the soft range of X-ray radiation (a); results for anatase thin films: titanium $L_{2,3}$ (b) and oxygen K (c) X-ray absorption edges collected in surface-sensitive total electron yield (TEY) mode, and Ti 2p (d) and O 1s (e) X-ray photoelectron spectra of the same film.

emitted photoelectrons at a given electron energy. The IMFP values were calculated using the QUASES-IMFP-TPP2M algorithm (Ver. 3.0, code written by Sven Tougaard, using the TPP-2M-Tanuma, Powell and Penn formula[40]). In the case of TiO_2 the results are 0.72 nm and 2.39 nm, at photon energies of 200 and 1200 eV above O 1s and Ti 2p peaks, respectively. It means that X-ray photoelectron spectra, collected at photon energies of 200 and 1200 eV above the O 1s and Ti 2p peaks as presented in Fig. 5, provide information on the chemical states of oxygen and titanium at the following sampling depths: 2.2 nm (surface) and 7.2 nm (subsurface).

High resolution oxygen 1s and titanium 2p X-ray photo-electron spectra for titanium oxide thin films with different phase compositions and stoichiometries are shown in Fig. 5. The oxygen 1s spectra were fitted with three components centred at 532.5 eV, 531.1 eV and 530.2 eV. As shown in the literature,[41–45] the assignment of O 1s peaks is debatable. The first and the second components at 532.5 eV, and 531.1 eV, respectively, are usually attributed to water, –OH groups chemisorbed at the surface or oxygen vacancies. This last interpretation seems to be incorrect as claimed in many papers.[42,45] However, the second component at 531 eV could be assigned to oxygen associated with Ti^{3+} species and is marked as O_V. The third peak is due to O^{2-} species occupying the TiO_2 lattice sites, hence denoted as O_{lat}. Titanium 2p spectra are fitted with 4 to 8 lines. For each sample, $2p_{1/2}$ and $2p_{3/2}$ doublet structures are visible due to the spin–orbit splitting of the 2p orbital. Main lines located at 464.4 and 458.6 eV originate from Ti^{4+} species present in TiO_2. Peaks centred at 462.8 and 457.4 eV are assigned to Ti^{3+} oxidation states. Peaks assigned to Ti^{2+}, located at 461.9 and 456.5 eV, are present in both the TiO spectra and the spectrum collected at 1660 eV for Ti_2O_3 thin films. The Ti 2p spectrum of TiO thin films collected at 1660 eV was fitted with 8 lines, with 2 additional peaks located at 459.9 and 454.8 eV, originating from Ti^0 species. Anatase and rutile samples, sputtered at higher oxygen partial pressures, exhibit neither Ti^{2+} nor Ti^0 peaks.

The results of integrated XPS fits are presented in Fig. 6. The Ti^{4+} contribution increases with the change in the crystallographic structure from TiO to TiO_2 in both subsurface and surface regions (Fig. 6a). The high amount of Ti^{4+} species is attributed to the formation of native titania, covering the surface of the thin films. Peaks originating from Ti^0 states, visible in the spectrum of TiO thin films collected at 1660 eV, disappear at 660 eV, where the sampling depth is shallower. Likewise, peaks assigned to Ti^{2+} states, present in the Ti 2p
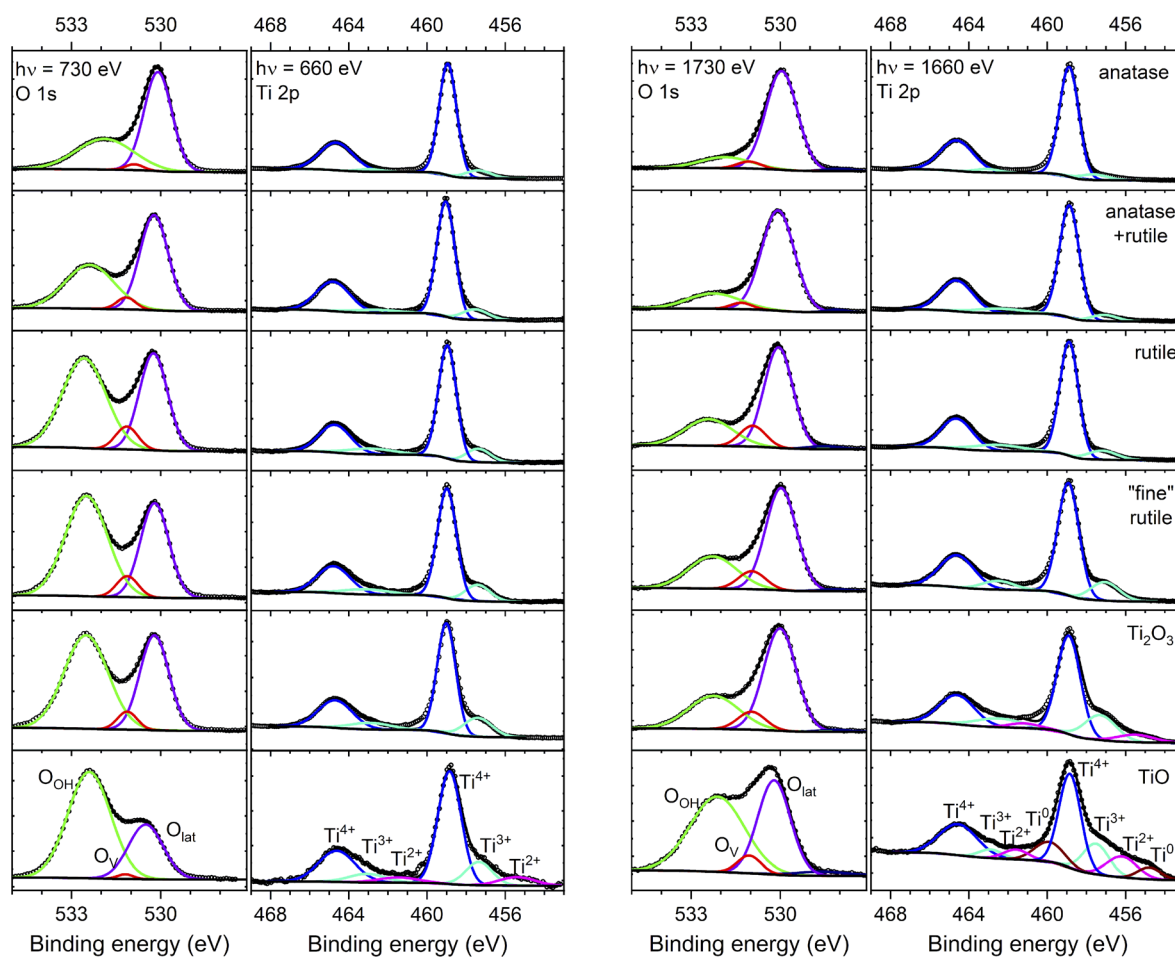

Fig. 5 High-resolution oxygen 1s and titanium 2p X-ray photoelectron spectra deconvoluted after Shirley background subtraction, collected at photon energies of 730, 660, 1730 and 1660 eV for titanium oxide thin films deposited by RF sputtering.
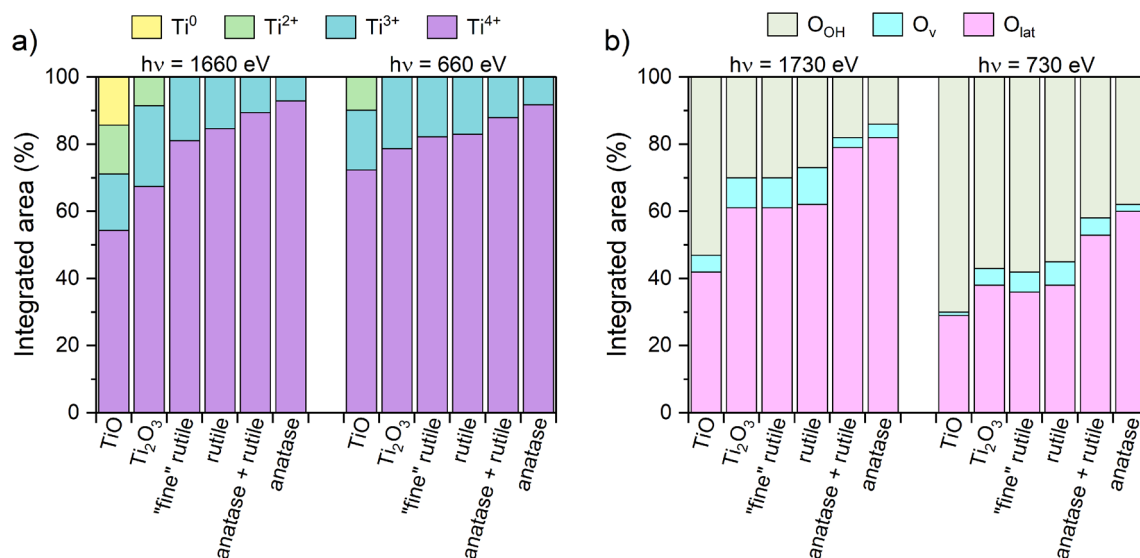
30196 | J. Mater. Chem. A, 2025, 13, 30191–30203

This journal is © The Royal Society of Chemistry 2025

Fig. 6 Integrated areas of XPS peaks based on Gaussian fitting of Ti 2p (a) and O 1s (b) spectra presented in Fig. 5.

spectrum collected at a photon energy of 1660 eV for Ti_2O_3 thin films, disappear in the more surface-sensitive spectrum. When the p_{O_2} is low (from 1.5 to 3.5×10^{-4} mbar) in the sputtering chamber, the amount of oxygen is insufficient to form stoichiometric TiO_2. Then, when such films are exposed to air, Ti atoms at the surface bind with oxygen from air, increasing their oxidation state. In contrast, the deeper layers might not be so easily oxidized; hence the amount of Ti^0, Ti^{2+} and Ti^{3+} species is higher in this case.

The analysis of O 1s spectra supports the proposed mechanism. The contribution of the 532.5 eV peak, assigned as O_{OH} in Fig. 5 and 6b, is higher in the case of the spectra collected at the lower photon energy for all thin films. The areas of the O_{OH} peaks are larger than those of the lattice peak (O_{lat}, located at 530.2 eV) not only in TiO and Ti_2O_3 spectra collected at 730 eV, but also for the fine-crystalline rutile sample. The area of this peak decreases significantly in the spectra collected at 1730 eV for all thin films. This relative change in the O_{lat} and O_{OH} peak areas upon increasing the probing depth demonstrates that O_{OH} represents species associated with the surface. Comparison with the Ti 2p spectra leads to the conclusion that the presence of O_{lat} species is related to Ti^{4+}, while the O_{OH} peak is more pronounced in thin films showing a more diversified Ti 2p spectral profile composed of Ti^0 and Ti^{2+} besides Ti^{3+} and Ti^{4+}.

The presence of Ti^{3+} lines in Ti 2p XPS for thin films obtained at high oxygen partial pressures (from 4.4 to 9.5×10^{-4} mbar) implies the formation of Ti^{3+} sites in the TiO_2 lattice, since XRD patterns did not reveal reflexes from the Ti_2O_3 phase (Fig. S3, in the SI). Each Ti^{3+} ion in otherwise stoichiometric rutile, anatase or mixed anatase/rutile TiO_2 leads to some imbalance in the ionic lattice.

Within the photon energy range of 200 to 1200 eV above the O 1s and Ti 2p peaks, the photoelectron signal emitted from the sample is strongly attenuated, limiting the probing depth to a few nm only. Increasing the sampling depth from 2.2 to 7.2 nm demonstrated significant differences between the

surface and sub-surface concentration of defects. However, this analysis is not applicable to the bulk of thin films.

Titanium $L_{2,3}$ and oxygen K X-ray absorption spectra collected in TEY and TFY modes for titanium oxide thin films are presented in Fig. 4b, c and Fig. 7. The titanium L X-ray absorption edge (Fig. 7a) is a result of $2p^6 3d^n \rightarrow 2p^5 3d^{n+1}$ transitions and consists of L_3 and L_2 contributions, originating from spin–orbit splitting of the 2p state into $2p_{3/2}$ and $2p_{1/2}$ levels. Further separation into two doublets is due to the crystal field splitting of the Ti 3d orbitals into low-energy (t_{2g}) and high-energy (e_g) parts, caused by bonding of Ti 3d states with O 2p states.[46] The e_g suborbitals are directed towards ligands and their hybridization is larger, which causes additional broadening of e_g peaks (peaks C and E) in contrast to t_{2g} peaks (B and D) as can be seen in Fig. 4b. In the case of anatase and rutile TiO_2, the L_3–e_g feature is additionally composed of two peaks (C1 and C2) due to long-range (1 nm length scale) effects in the TiO_2 structure.[47,48] The L_3 onset, marked with arrows in Fig. 7a, moves towards higher energies for samples deposited at the increased oxygen flow rate η_{O_2}. The difference is approximately 0.7 eV per oxidation state. This effect was observed in the bulk-sensitive total fluorescence yield mode, only.

The difference between the surface and bulk electronic structure is visible in the XAS results. The first major difference is that the onset of the Ti L_3 edge detected in TFY mode is shifted towards lower energies in the case of TiO and Ti_2O_3 thin films, as well as fine-crystalline rutile (Fig. 7a), by 0.5–0.7 eV per oxidation state in the bulk. This effect has been observed previously,[49,50] where the shift was reported to be 1.5–2.0 eV per oxidation state.

The oxygen K absorption spectra (Fig. 7b) of titanium oxides originate from $1s \rightarrow 2p$ transitions[51] and consist of a few features that can be divided into a low-energy region (528–536 eV, marked as blue) and a high-energy region (536–550 eV, marked as pink). The first part comprises two peaks. One, centred at 530.9 eV, is ascribed to $1s \rightarrow t_{2g}$, while the second,

This journal is © The Royal Society of Chemistry 2025

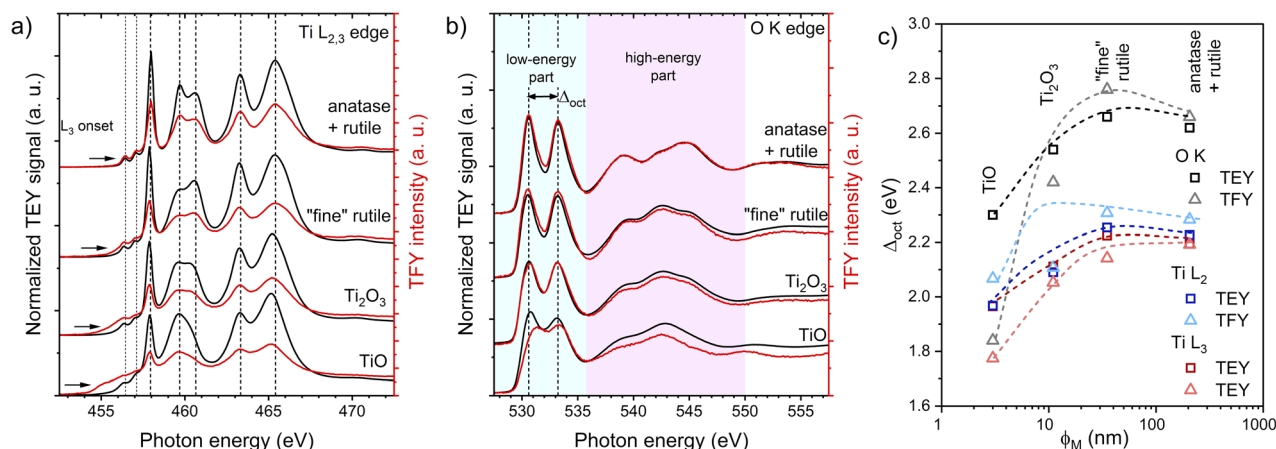*J. Mater. Chem. A*, 2025, **13**, 30191–30203 | **30197**

Fig. 7 Titanium $L_{2,3}$ (a) and oxygen K (b) edge X-ray absorption spectra after background subtraction, collected in TEY (black) and TFY (red) modes for TiO, Ti_2O_3 and TiO_2 thin films with main line positions marked. Crystal field splitting Δ_{oct} calculated as a difference in positions of e_g and t_{2g} peaks based on O K and Ti $L_{2,3}$ spectra in TEY and TFY modes (c) for thin films with different ϕ_M.

centred at 533.6 eV, corresponds to 1s → e_g transitions. This part of the spectrum originates from the hybridization of O 2p orbitals with Ti 3d bands (empty in the case of TiO_2).[52] Both peaks become narrower as the structure of the thin films changes from TiO through Ti_2O_3, and finally to TiO_2, which is caused by the increase in valency of Ti from Ti^{2+} to Ti^{3+} and Ti^{4+}.[53] Because Ti^{2+} has 2 electrons in the low-energy sub-orbitals of the 3d band (3d-t_{2g}), both the density of unoccupied 3d states and the probability of transition from oxygen 1s to these unoccupied states are lower than in the case of Ti^{4+}. The features visible within the range of 536–550 eV are due to the hybridization of O 2p with the 4sp band, and are attributed to 1s → $3a_{1g}, 4t_{1u}$ transitions.[51] In contrast to the 3d band, the 4sp band is not sharply structured, which leads to overlapping, broadened peaks,[52] as can be seen in the high-energy region of the O K spectra (Fig. 7b).

The crystal field splitting Δ_{oct} was calculated as the difference between the e_g and t_{2g} peaks for the Ti $L_{2,3}$ and O K edges collected in TEY and TFY modes (Fig. 7c). In the case of the Ti L_3 edge, determination of Δ_{oct} is not straightforward due to the splitting of e_g into d_{z^2} and $d_{x^2-y^2}$ states, which causes asymmetry in the spectral shape. The calculated values increase from 1.7–2.1 eV to 2.2–2.3 eV with the increase in ϕ_M as the valence state of Ti atoms changes from 2 to 4. The crystal field splitting calculated from the O K spectra is also presented in Fig. 7c. The values are higher than those calculated from the Ti $L_{2,3}$ spectra, and are in better agreement with the values found in the literature (2.4 eV for Ti_2O_3 and 2.6 eV for TiO_2 (ref. 52)).

Interaction with light – CPD from Kelvin probe and photocurrent measurements

The contact potential difference, CPD measured using a Kelvin probe, is a surface sensitive technique that allows for probing changes in the work function of, e.g., semiconductors.[54] When an n-type semiconductor such as TiO_2 is illuminated with UV radiation above its fundamental band gap, the work function decreases because of an upward shift in the Fermi level. Thus,

the process of electron extraction is facilitated resulting in an increased concentration of holes in the near-surface layer. It has therefore been claimed[54] that a larger change in the work function upon illumination correlates positively with the enhanced photocatalytic activity.

Changes in contact potential difference (ΔCPD) were calculated as the difference between CPD upon illumination (CPD_{ill}) and in the dark (CPD_{dark}) according to the equation:

$$\Delta CPD = CPD_{ill} - CPD_{dark} \tag{5}$$

The relationship between ΔCPD and surface photovoltage (SPV):[55]

$$SPV = -\Delta CPD \tag{6}$$

is of a particular interest in this study. Positive sign of SPV upon UV illumination is characteristic for n-type semiconductors. The experimental results of the contact potential difference (CPD) provide information about the interaction of light with thin films of titanium oxides as illustrated in Fig. 8a.

As demonstrated in Fig. 8a, following a sharp decrease in the contact potential difference CPD caused by illumination with 370 nm light ($h\nu = 3.35$ eV), a slight increase in the CPD can be seen, which gradually stabilises. Upon UV light illumination, the CPD of titanium dioxide thin films reaches a plateau within 30 minutes. Upon switching off the illumination, a subsequent rise in CPD is observed, with the signal gradually returning to its initial level. The duration of the recovery period was approximately 30 minutes.

Moreover, the higher SPV observed for thin films with the lowest conductivity and the highest figure of merit correlates with their highest photoactivity as shown in Fig. 8b.

The primary goal is the identification of semiconductor materials which, when used as photoelectrodes in a PEC cell, are capable of dissociating water using photogenerated charge carriers, even without the need for an external bias. However, from the perspective of materials research and development, it
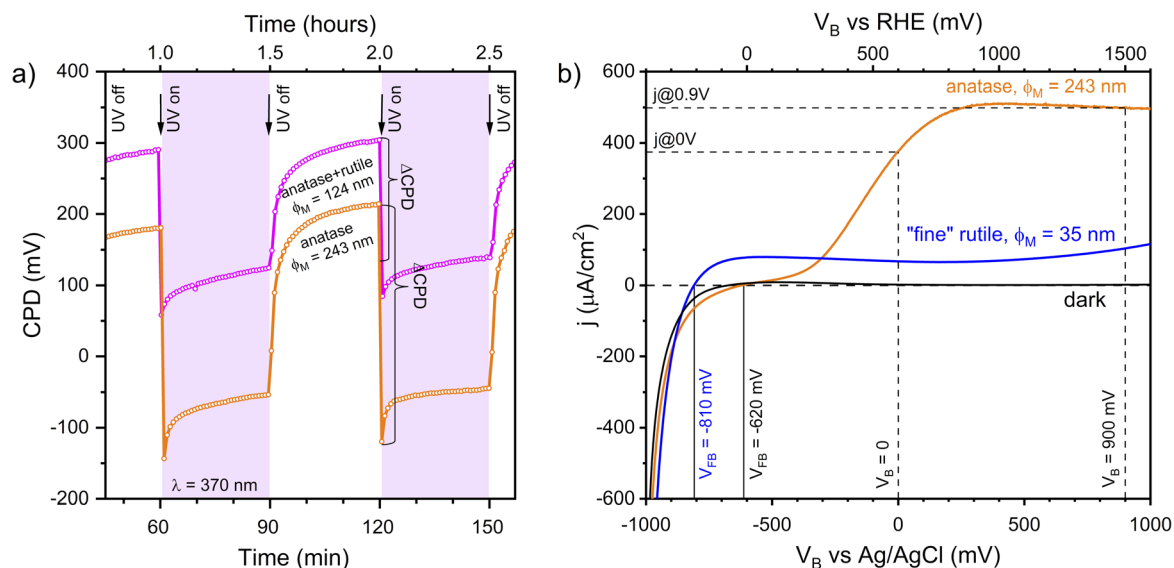
30198 | J. Mater. Chem. A, 2025, **13**, 30191–30203

This journal is © The Royal Society of Chemistry 2025

Fig. 8 Contact potential difference CPD *vs.* time for rutile/anatase and anatase thin films with changes under 370 nm illumination (ΔCPD) marked (a); current density *j* as a function of applied bias voltage V_B in PEC (b).

is imperative to evaluate the fundamental properties of the photoelectrode, including its ability to generate photocurrent at a specific potential. This is assessed based on the dependence of the current density, j, on the applied voltage, V_B, with and without illumination. Furthermore, j–V_B analysis has been demonstrated to be useful to estimate the flat band potential (V_{FB}). V_{FB} is defined as an applied potential causing disappearance of the bending of the bands formed at the semiconductor–electrolyte interface. This is known as the onset of photocurrent, and V_{FB} should take negative values.

Fig. 8b presents the j–V_B characteristics demonstrating the fundamental photoelectrochemical properties of thin-film electrodes that vary with the phase composition and microstructure. The graph also shows the photocurrent values at selected potentials V_B, *i.e.*, 0 mV and 900 mV *vs.* Ag/AgCl reference electrode. The flat band potential V_{FB} of the "fine" rutile (ϕ_M = 35 nm) photoanode was more negative (V_{FB} = −810 mV) than that of the anatase-based photoanode (ϕ_M = 243 nm, V_{FB} = −620 mV). However, the latter achieved much higher photocurrent density at the selected V_B voltages (of about 400 µA cm^{-2} at 0 mV and 500 µA cm^{-2} at 900 mV).

Additionally, the shape and fill factors affect the photoelectrochemical performance. The fill factor (FF) for photoelectrochemical cells and photovoltaic systems is a pivotal parameter that determines not only the "squareness" of the current–voltage curve, but also the efficiency of the device in converting light into electricity.

These parameters can be calculated from the j–V_B characteristics. In the case of the shape factor, the ratio of the photocurrent at two values of the applied potential, *i.e.*, 0 V and 900 mV with respect to the Ag/AgCl electrode is considered. For the fill factor, data related to the maximum power are utilized. The values of these parameters depend on the geometry of the current–voltage characteristics in the illuminated state and the

highest values of the photocurrent in the applied voltage range. The highest shape factor of about 0.9 was obtained for a PEC cell with a photoanode in the form of a thin layer of "fine" rutile. The optimal fill factor values of approximately 0.6 are exhibited by well-crystallized TiO$_2$ layers that are a mixture of anatase and rutile or pure anatase.

Fig. 9a shows the surface photovoltage (SPV) results for titanium oxide thin films obtained at different values of the parameter ϕ_M. For the TiO thin film, no response to the UV illumination was detected, which means no surface photovoltage was generated (SPV = 0 mV). This is due to the metallic character of TiO. The lowest value of 20 mV was observed for Ti$_2$O$_3$ thin films, while the highest values of approximately 270 mV were displayed by TiO$_2$ with an anatase structure or with a large anatase content (74–90%). The surface photovoltage is induced by the illumination of the semiconductor surface and the associated change in the surface potential equilibrium, followed by charge transfer. The driving force behind the charge transfer is the surface generated electric field in the semiconductor. When photons with an energy equal to or greater than the band gap energy of a semiconductor act on the surface of the semiconductor, the resulting photocarriers (electron–hole pairs) can be transported in opposite directions under the influence of the electric field. A change in the surface charge density results in a decrease in the surface potential. In the case of an n-type semiconductor, the electric field causes electrons to move into the material and holes to move towards the surface. The sign of the change in the CPD signal when photons with energy close to the band gap are applied is related to the conduction type of the semiconductor. In the case of an n-type semiconductor, as the CPD decreases upon illumination (Fig. 8a), the sign of the SPV becomes positive. All the semiconductors studied here show a positive sign of surface photovoltage associated with n-type conductivity. The increase in
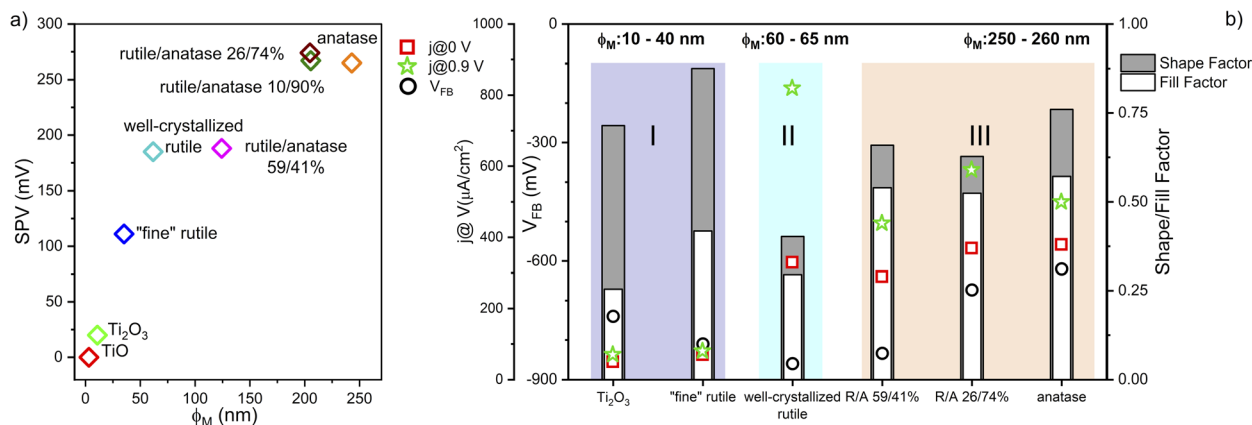
This journal is © The Royal Society of Chemistry 2025

J. Mater. Chem. A, 2025, **13**, 30191–30203 | **30199**

Fig. 9 Surface photovoltage SPV ($=-\Delta$CPD) under 370 nm illumination as a function of figure of merit ϕ_M for thin films of different phase compositions (a) and the analysis of the most important parameters of PEC performance, V_{FB} – flat band potential, j – current density upon white light illumination, shape and fill factor (b).

SPV observed during the transition from TiO to TiO$_2$ *via* Ti$_2$O$_3$ can be attributed to an increase in the value of the band gap.

As illustrated in Fig. 9b, a comprehensive overview of the photoelectrochemical parameters obtained for photoanodes is provided, with the electronic, structural and microstructural properties of these photoanodes thoroughly examined in this work. Considering all photoelectrochemical parameters such the flat band potential, photocurrent density, shape and fill factors, it is possible to distinguish three classes of photoanode materials. This type of classification is based on the increasing figure of merit Φ_M defined by eqn (3). The class I with the lowest figure of merit Φ_M between 10 and 40 nm comprises Ti$_2$O$_3$ and "fine" rutile. The photoanodes of this class display relatively high V_{FB} values but low photocurrent density. The shape and fill factor are quite high. Class II (medium Φ_M = 60–65 nm) contains well-crystallised rutile TiO$_2$, only. This is an example of the photoanode with the highest photocurrent density at 900 mV but the lowest shape factor because the j–V_B characteristics do not saturate. This can be attributed to significant differences between the photocurrents at 0 V and 900 mV, which may be related to the enhanced recombination of photogenerated charge carriers.[56]

Class III represents the best choice of photoanode materials that correspond to the highest Φ_M = 250–260 nm. This class contains a mixture of anatase and rutile TiO$_2$ as well as pure anatase. Photoanodes belonging to this class demonstrate relatively high photocurrent density and shape factor but poor flat band potential. Therefore, considering class III as the best choice for TiO$_2$ photoanode materials is a result of a compromise between these fundamental photoelectrochemical parameters.

It is well known that the photoelectrochemical performance of thin film photoelectrodes is affected to a large extent by their microstructure. The dynamics of charge carriers is particularly susceptible to the formation of conduction channels, the best example of which are nanowires or nanotubes. In the case of thin films deposited by sputtering, columnar growth is frequently encountered.[57] The shape and size of these columns

depend critically on the sputtering conditions such as time, substrate temperature, substrate bias and sputtering rate.[58–61] Scanning electron microscopy, SEM applied to the series of thin films discussed in this work reveals the evolution of microstructure as shown in Fig. 10a.

As can be observed in cross-sectional SEM images (Fig. 10a), all thin film photoanodes grow in columns, irrespective of the oxygen content in the reactive gas mixture. However, the shape and size of columns change when the oxygen to argon ratio is varied. The morphology of TiO and Ti$_2$O$_3$ is characterized by straight, narrow columns, whose diameter does not change as the layers grow perpendicular to the substrate. This type of growth mechanism is also observed in the case of a fine-crystalline rutile thin film. As a result of substrate heating, the columns are not densely packed, and free spaces can be seen between them. With an increase in oxygen partial pressure during sputtering, rutile crystallizes. The shape of the columns changes from straight to a "V" form: very narrow at the bottom of the layer and broadened at the top, near the surface. This behaviour is further observed in TiO$_2$ layers of mixed rutile/anatase and pure anatase structures. The columns at the bottom of well-crystallized layers are short and narrow due to the widening of the growing columns, which take more space as the layer's thickness increases, and inhibit expansion of the remaining "grains". Such inhomogeneity along the layer thickness is typical of the competitive texture zone according to the structure zone model proposed by Barna and Adamik for thin films.[58]

A schematic representation of three different classes of Ti–O, distinguished based on their photoelectrochemical behaviour (Fig. 9b), is presented in Fig. 10b in the context of microstructure and defect structure. This scheme summarizes the results of this work and indicates the correlation between the conditions of growth and distribution of defects as determined from surface and subsurface XPS studies. The overall concentration of OH–Ti^{3+} defects, including both surface and subsurface ones, decreases as the films are deposited at higher oxygen levels (this is also related to the increase in the figure of merit). However,
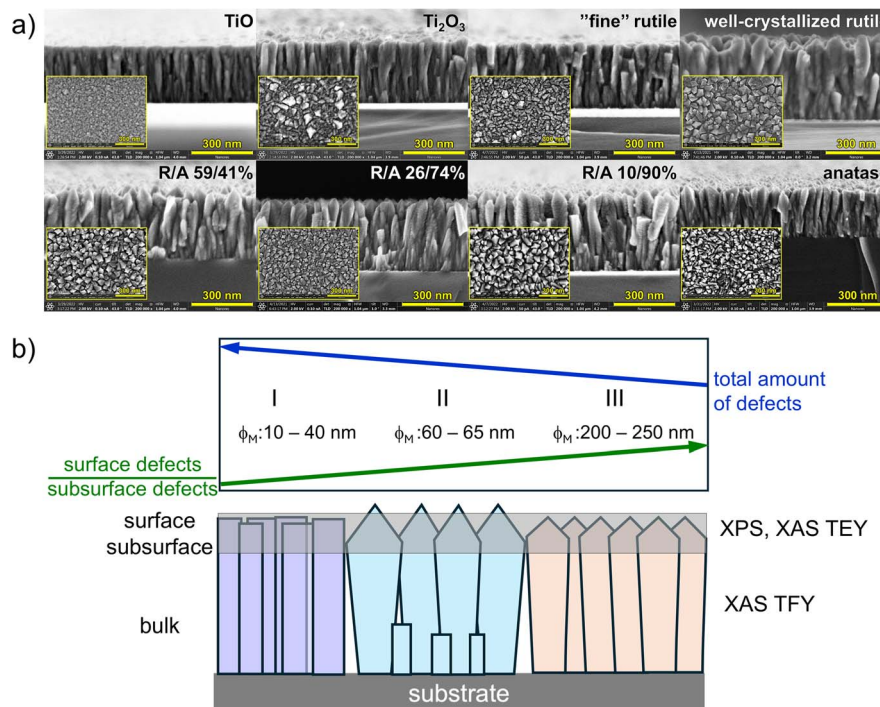
30200 | *J. Mater. Chem. A*, 2025, **13**, 30191–30203

This journal is © The Royal Society of Chemistry 2025

Fig. 10 Scanning electron microscopy cross-sectional images and top views of titanium oxide thin films obtained *via* reactive RF magnetron sputtering (a). Schematic representation of three different classes of Ti–O photoanodes (b).

concerning the distribution of these defects in depth, it can be seen that the surface-to-subsurface concentration of OH–Ti^{3+} increases when the oxygen-to-argon ratio increases. The presence of surface defects has been claimed be beneficial for improved water splitting efficiency[62] and correlates well with the optimized performance of thin film photoanodes that belong to class III (with the highest figure of merit) as shown in Fig. 9b.

Therefore, the selection of photoanode material is determined by achieving a consensus between all photoelectrochemical parameters. The requirements are met by photoanodes with a crystallographic structure of anatase or a mixture of anatase and rutile.

Conclusions

The research presented in this paper focuses on the deposition and investigation of surface *versus* bulk properties of TiO$_x$ thin films, aimed at their application as photoanodes for green hydrogen generation by water splitting in a self-made photoelectrochemical cell. Applying a set of surface- and bulk-sensitive techniques enabled the analysis of optical, microstructural and electronic properties of the synthetized layers. Differentiation between surface and bulk properties and their respective contributions towards the mechanism of photoelectrochemical water splitting was achieved by using XPS and XAS techniques based on synchrotron radiation, performed in two distinct modes. XPS carried out at different photon energies allows for studying oxygen and titanium valence states at the surface and subsurface, finally resulting in the determination of OH–Ti^{3+} defect depth distribution. Two modes of XAS,

surface sensitive TEY and bulk probing TFY, enabled monitoring of the oxidation process of thin films as a function of gas composition in the Ar + O$_2$ mixture. Contact potential difference, CPD measured using a Kelvin probe as a surface sensitive technique allowed for probing changes in the work function upon UV illumination and correlating them positively with the photocurrent density in the PEC cell. All photoanodes demonstrated negative values of the flat band potential, which varied from −880 to −600 mV. The highest values of the photocurrent at $V_B = 0$ mV and $V_B = 900$ mV were obtained for thin films of well-crystallized rutile, mixtures of anatase and rutile, and pure anatase. Photoanodes based on Ti$_2$O$_3$ and fine rutile achieved the lowest photocurrent values despite very good V_{FB} values.

Three different classes of photoanodes were identified. They are distinguished by the figure of merit introduced to find a compromise between electrical resistivity and the absorption coefficient. Photoanodes consisting of an anatase–rutile mixture or pure anatase, which belong to class III with the highest figure of merit exhibited the best photoelectrochemical performance, representing a consensus between all photoelectrochemical parameters. This effect has been attributed to both the microstructure and the favourable OH–Ti^{3+} defect distribution at the film surface.

Data availability

The data supporting this article have been included as part of the SI. Data are stored in RODBUK Cracow Open Research Data Repository **https://home.rodbuk.pl/en**.

This journal is © The Royal Society of Chemistry 2025

J. Mater. Chem. A, 2025, **13**, 30191–30203 | **30201**

The Supplementary information contains details on the growth conditions and thin film basic parameters (Table S1), XPS carbon 1s spectra (Fig. S1), current *vs.* potential curves at three different Kelvin probe distances from the sample (Fig. S2), GIXRD patterns of TiO_x thin films deposited by RF sputtering from metallic Ti target at different oxygen partial pressures (Fig. S3), and spectral dependence of the absorption coefficient calculated from the eqn (2) (Fig. S4). See DOI: **https://doi.org/10.1039/d5ta03441h**.

Author contributions

Conflicts of interest

There are no conflicts to declare.

Acknowledgements

References

1 F. Cao, J. Xiong, F. Wu, Q. Liu, Z. Shi, Y. Yu, X. Wang and L. Li, *ACS Appl. Mater. Interfaces*, 2016, **8**, 12239–12245.

2 M. D. P. A. Shakya, K. M. D. C. Jayathilaka, W. T. R. S. Fernando, W. T. M. A. P. K. Wanninayake, L. S. R. Kumara, O. Seo, J. Tang, O. Sakata, W. P. Siripala and R. P. Wijesundera, *Crystals*, 2024, **15**, 28.

3 B. D. Alexander, P. J. Kulesza, I. Rutkowska, R. Solarska and J. Augustynski, *J. Mater. Chem.*, 2008, **18**, 2298.

4 H. Han, P. Anushkkaran, J. S. Jang, J. H. Yu, J. H. Park and T. W. Kim, *J. Power Sources*, 2025, **641**, 236808.

5 Y.-S. Hu, A. Kleiman-Shwarsctein, A. J. Forman, D. Hazen, J.-N. Park and E. W. McFarland, *Chem. Mater.*, 2008, **20**, 3803–3805.

6 F. F. Abdi, T. J. Savenije, M. M. May, B. Dam and R. van de Krol, *J. Phys. Chem. Lett.*, 2013, **4**, 2752–2757.

7 M. Zukalová, A. Zukal, L. Kavan, M. K. Nazeeruddin, P. Liska and M. Grätzel, *Nano Lett.*, 2005, **5**, 1789–1792.

8 I. Cesar, K. Sivula, A. Kay, R. Zboril and M. Grätzel, *J. Phys. Chem. C*, 2009, **113**, 772–782.

9 K. Keis, E. Magnusson, H. Lindström, S.-E. Lindquist and A. Hagfeldt, *Sol. Energy Mater. Sol. Cells*, 2002, **73**, 51–58.

10 D. Carta, G. Mountjoy, A. Regoutz, A. Khiat, A. Serb and T. Prodromakis, *J. Phys. Chem. C*, 2015, **119**, 4362–4370.

11 Z. N. Kayani, Z. Khalid, S. Riaz and S. Naseem, *Ceram. Int.*, 2025, **51**, 1405–1423.

12 D. A. H. Hanaor and C. C. Sorrell, *J. Mater. Sci.*, 2011, **46**, 855–874.

13 Y. Li, Y. Yang, X. Shu, D. Wan, N. Wei, X. Yu, M. B. H. Breese, T. Venkatesan, J. M. Xue, Y. Liu, S. Li, T. Wu and J. Chen, *Chem. Mater.*, 2018, **30**, 4383–4392.

14 T. Bak, J. Nowotny, M. Rekas and C. C. Sorrell, *Int. J. Hydrogen Energy*, 2002, **27**, 991–1022.

15 B. Bakbolat, C. Daulbayev, F. Sultanov, R. Beissenov, A. Umirzakov, A. Mereke, A. Bekbaev and I. Chuprakov, *Nanomaterials*, 2020, **10**, 1790.

16 M. Radecka, A. Kusior, A. Trenczek-Zajac and K. Zakrzewska, Chapter Four – Oxide Nanomaterials for Photoelectrochemical Hydrogen Energy Sources, in *Adv. Inorg. Chem.*, ed. R. van Eldik and W. Macyk, Academic Press, 2018, pp. 145–183.

17 J. Li and N. Wu, *Catal. Sci. Technol.*, 2015, **5**, 1360–1384.

18 M. Radecka, M. Rękas and K. Zakrzewska, *Trends Inorg. Chem.*, 2006, **9**, 81–126.

19 K. Zakrzewska, K. Kollbek, M. Sikora, C. Kapusta, J. Szlachetko, M. Sitarz, M. Ziabka and M. Radecka, *Int. J. Hydrogen Energy*, 2015, **40**, 815–824.

20 T. Jafari, E. Moharreri, A. S. Amin, R. Miao, W. Song and S. L. Suib, *Molecules*, 2016, **21**, 900.

21 S. Corby, R. R. Rao, L. Steier and J. R. Durrant, *Nat. Rev. Mater.*, 2021, **6**, 1136.

22 A. J. Gardecka, C. Bishop, D. Lee, S. Corby, I. P. Parkin, A. Kafizas and S. Krumdieck, *Appl. Catal., B*, 2018, **224**, 904–911.

23 Y. Luo and H. Lee, *Nano-Micro Lett.*, 2021, **13**, 45.

24 T. S. Rajaramana, S. P. Parikh and V. G. Gandhi, *Chem. Eng. J.*, 2020, **389**, 123918.

25 X. Chen, L. Liu, P. Y. Yu and S. S. Mao, *Science*, 2011, **331**, 746–750.

26 K. Zhang, L. Wang, J. K. Kim, M. Ma, G. Veerappan, C.-L. Lee, K. Kong, H. Lee and J. H. Park, *Energy Environ. Sci.*, 2016, **9**, 499–503.

27 H. M. Hwang, S. Oh, J.-H. Shim, Y.-M. Kim, A. Kim, D. Kim, J. Kim, S. Bak, Y. Cho, V. Q. Bui, T. A. Le and H. Lee, *ACS Appl. Mater. Interfaces*, 2019, **11**, 35693–35701.

28 K. Zakrzewska, A. Brudnik, M. Radecka and W. Posadowski, *Thin Solid Films*, 1999, **343–344**, 152–155.

29 J. Rodríguez, M. Gómez, J. Ederth, G. A. Niklasson and C. G. Granqvist, *Thin Solid Films*, 2000, **365**, 119–125.

30 R. Swanepoel, *J. Phys. E: Sci. Instrum.*, 1983, **16**, 1214–1222.

31 D. C. Grinter, P. Ferrer, F. Venturini, M. A. van Spronsen, A. I. Large, S. Kumar, M. Jaugstetter, A. Iordachescu, A. Watts, S. L. M. Schroeder, A. Kroner, F. Grillo, S. M. Francis, P. B. Webb, M. Hand, A. Walters,

30202 | *J. Mater. Chem. A*, 2025, **13**, 30191–30203

This journal is © The Royal Society of Chemistry 2025

M. Hillman and G. Held, *J. Synchrotron Radiat.*, 2024, **31**, 578–589.

32 R. Singh, M. Gupta, D. M. Phase and S. K. Mukherjee, *Mater. Res. Express*, 2019, **6**, 116449.

33 A. Vahl, S. Veziroglu, B. Henkel, T. Strunskus, O. Polonskyi, O. C. Aktas and F. Faupel, *Materials*, 2019, **12**, 2840.

34 M. Selmi, F. Chaabouni, M. Abaab and B. Rezig, *Phys. Status Solidi C*, 2008, **5**, 3368–3372.

35 M. Quesada-Gonzalez, B. A. D. Williamson, C. Sotelo-Vazquez, A. Kafizas, N. D. Boscher, R. Quesada-Cabrera, D. O. Scanlon, C. J. Carmalt and I. P. Parkin, *J. Phys. Chem. C*, 2018, **122**, 714–726.

36 L. Weinhardt, D. Hauschild and C. Heske, *Adv. Mater.*, 2019, **31**, 180660.

37 M. van der Merwe, R. Garcia-Diez, L. Lahn, R. E. Wibowo, J. Frisch, M. Gorgoi, W. Yang, S. Ueda, R. G. Wilks, O. Kasian and M. Bär, *ACS Catal.*, 2023, **13**, 15427–15438.

38 V. Prusakova, C. Collini, M. Nardi, R. Tatti, L. Lunelli, L. Vanzetti, L. Lorenzelli, G. Baldi, A. Chiappini, A. Chiasera, D. Ristic, R. Verucchi, M. Bortolotti and S. Dirè, *RSC Adv.*, 2017, **7**, 1654–1663.

39 W. R. Flavell, *Faraday Discuss.*, 2022, **236**, 9–57.

40 S. Tanuma, C. J. Powell and D. R. Penn, *Surf. Interface Anal.*, 1993, **21**, 165–176.

41 M. J. Jackman, A. G. Thomas and C. Muryn, *J. Phys. Chem. C*, 2015, **119**, 13682–13690.

42 T. J. Frankcombe and Y. Liu, *Chem. Mater.*, 2023, **35**, 5468–5474.

43 S. Kucharski, P. Ferrer, F. Venturini, G. Held, A. S. Walton, C. Byrne, J. A. Covington, S. K. Ayyala, A. M. Beale and C. Blackman, *Chem. Sci.*, 2022, **13**, 6089–6097.

44 L. Liccardo, M. Bordin, P. M. Sheverdyaeva, M. Belli, P. Moras, A. Vomiero and E. Moretti, *Adv. Funct. Mater.*, 2023, **33**, 2212486.

45 H. Idriss, *Surf. Sci.*, 2021, **712**, 121894.

46 F. M. F. De Groot, J. Faber, J. J. M. Michiels, M. T. Czyżyk, M. Abbate and J. C. Fuggle, *Phys. Rev. B: Condens. Matter Mater. Phys.*, 1993, **48**, 2074–2080.

47 P. Krüger, *J. Phys.: Conf. Ser.*, 2009, **190**, 012006.

48 J. P. Crocombette and F. Jollet, *J. Phys.: Condens. Matter*, 1994, **6**, 10811–10821.

49 G. S. Henderson, F. M. F. De Groot and B. J. A. Moulton, *Rev. Mineral. Geochem.*, 2014, **78**, 75–138.

50 E. Stoyanov, F. Langenhorst and G. Steinle-Neumann, *Am. Mineral.*, 2007, **92**, 577–586.

51 L. A. Grunes, R. D. Leapman, C. N. Wilker, R. Hoffmann and A. B. Kunz, *Phys. Rev. B: Condens. Matter Mater. Phys.*, 1982, **25**, 7157–7173.

52 F. M. F. De Groot, M. Grioni, J. C. Fuggle, J. Ghijsen, G. A. Sawatzky and H. Petersen, *Phys. Rev. B: Condens. Matter Mater. Phys.*, 1989, **40**, 5715–5723.

53 F. Frati, M. O. J. Y. Hunault and F. M. F. De Groot, *Chem. Rev.*, 2020, **120**, 4056–4110.

54 A. Torras-Rosell, S. R. Johannsen, K. Dirscherl, S. Daviðsdóttir, C. S. Jeppesen, S. Louring and I. H. Andersen, *Environ. Sci. Pollut. Res.*, 2017, **24**, 12683–12690.

55 D. Cavalcoli, B. Fraboni and A. Cavallini, in *Semiconductors and Semimetals*, ed. L. Romano, V. Privitera and C. Jagadish, Elsevier, 2015, vol. 91, pp. 251–278.

56 K. Płacheta, A. Kot, J. Banas-Gac, M. Zając, M. Sikora, M. Radecka and K. Zakrzewska, *Appl. Surf. Sci.*, 2023, **608**, 155046.

57 J. Banas-Gac, M. Radecka, A. Czapla, E. Kusior and K. Zakrzewska, *Appl. Surf. Sci.*, 2023, **616**, 156394.

58 P. B. Barna and M. Adamik, *Thin Solid Films*, 1998, **317**, 27–33.

59 B. Henkel, A. Vahl, O. C. Aktas, T. Strunskus and F. Faupel, *Nanotechnology*, 2018, **29**, 35703.

60 Q. Jiang, D. Ma, Y. Li and C. Chen, *Materials*, 2023, **16**, 7294.

61 A. Vahl, J. Dittmann, J. Jetter, S. Veziroglu, S. Shree, N. Ababii, O. Lupan, O. C. Aktas, T. Strunskus, E. Quandt, R. Adelung, S. K. Sharma and F. Faupel, *Nanotechnology*, 2019, **30**, 235603.

62 H. Kong, H. Yang, J.-S. Park, W.-S. Chae, H. Y. Kim, J. Park, J. H. Lee, S. Y. Choi, M. Park, H. Kim, Y. Song, H. Park and J. Yeo, *Adv. Funct. Mater.*, 2022, **32**, 2204106.

This journal is © The Royal Society of Chemistry 2025

J. Mater. Chem. A, 2025, **13**, 30191–30203 | **30203**